MDPI

Technical Note

Comparison of ASI-PRISMA Data, DLR-EnMAP Data, and Field Spectrometer Measurements on "Sale 'e Porcus", a Salty Pond (Sardinia, Italy)

Massimo Musacchio [1],*, Malvina Silvestri [1], Vito Romaniello [1], Marco Casu [2,3], Maria Fabrizia Buongiorno [1] and Maria Teresa Melis [2]

1. Istituto Nazionale di Geofisica e Vulcanologia, Osservatorio Nazionale Terremoti, Via di Vigna Murata 605, 00143 Roma, Italy; malvina.silvestri@ingv.it (M.S.); vito.romaniello@ingv.it (V.R.); fabrizia.buongiorno@ingv.it (M.F.B.)
2. Department of Chemical and Geological Sciences, Cittadella Universitaria (Blocco A)-S.S. 554 Bivio per Sestu, 09042 Monserrato, CA, Italy; marco.casu4@unica.it (M.C.); titimelis@unica.it (M.T.M.)
3. Department of Earth Sciences (DES), La Sapienza Università di Roma—Piazzale Aldo Moro 5, 00185 Rome, Italy
* Correspondence: massimo.musacchio@ingv.it; Tel.: +39-06-51-860-618

Abstract: A comparison between the ASI-PRISMA (Agenzia Spaziale Italiana-PRecursore IperSpettrale della Missione Applicativa) DLR-EnMAP (German Aerospace Center—Environmental Mapping and Analysis Program) data and field spectrometer measurements has been performed. The test site, located at the "Sale 'e Porcus" pond (hereafter SPp) in Western Sardinia, Italy, offers particularly homogenous characteristics, making it an ideal location not only for experimentation but also for calibration purposes. Three remote-sensed data acquisitions have been performed by these agencies (ASI and DLR) starting on 14 July 2023 and continuing until 22 July 2023. The DLR-EnMAP data acquired on 22 July overestimates both that of the ASI-PRISMA and the 14 July DLR-EnMAP radiance in the VNIR region, while all the datasets are close to each other, up to 2500 nm, for all considered days. The average absolute mean difference between the reflectance values estimated by the ASI-PRISMA and DLR-EnMAP, in the test area, is around 0.015, despite the small difference in their time of acquisition (8 days); their maximum relative difference value occurs at about 2100 nm. In this study, we investigate the relationship between the averaged ground truth value of reflectance, acquired by means of a portable ASD FieldSpec spectoradiometer, characterizing the test site and the EO reflectance data derived from the official datasets. FieldSpec measurements confirm the quality of both the ASI-PRISMA and DLR-EnMAP's reflectance estimations.

Keywords: ASI-PRISMA; DLR-EnMAP; ground truth; surface reflectance

1. Introduction

New orbiting hyperspectral missions, dedicated to the Earth's observation, are improving the observational capability of their user communities. Since the launch of the ASI-PRISMA sensor (2019), and with the DLR-EnMAP's launch (2022), our capability to exploit surface characterization has increased. The identification and extraction of surface features depend on established algorithms and processing methodologies tailored to various application domains, including geology [1], agriculture [2], water management [3,4], inland and coastal water monitoring [5], gas emission retrieval [6,7], and fire detection [8]. In 2019, the Italian Space Agency introduced a hyperspectral imaging platform called PRecursore Iperspettrale della Missione Applicativa (PRISMA) [9–13]. An assessment of its radiometric performance and accuracy in retrieving surface reflectance values has been conducted as detailed in [14]. The German Aerospace Center (Deutsches Zentrum für Luft- und Raumfahrt; DLR) launched the DLR-EnMAP (Environmental Mapping and Analysis

Program) [15,16] in 2022 and its performance is here compared with the Italian sensor. To evaluate satellite acquisitions, proximal spectral measurements have been conducted in quasi-coincidence with the collection of space data on the Sale 'e Porcus pond using field hyperspectral radiometers [17]; indeed, the use of ground truth data is necessary to distinguish different materials on the Earth's surface. A comparison between the spectral signatures acquired from space and the ground represents the proper way to identify the minerals composing the SPp by means of hyperspectral remote-sensed data processing techniques for land, mineral, and bare soil applications, which have been developed since the early 70s [18,19]. In the above-mentioned domains, the availability of a continuous spectrum enhances the effectiveness of algorithms in identifying particular absorption features and enables an improved retrieval of surface properties [20–22]. In this paper, we compared the performance of the standard L2 TOA reflectance products provided by the agencies (ASI for PRISMA and DLR for EnMAP) [23,24] in the range 0.4–2.5 um with ground truth data acquired on 18 July 2023 on the SPp. This area is covered by compositionally homogeneous evaporites and is also characterized by a very flat topography, suitable for field spectrometer measurements.

2. Materials and Methods

DLR-EnMAP and ASI-PRISMA are two Earth observation satellites that capture hyperspectral data for various applications, including environmental monitoring, agriculture, and land use mapping. While they share some similarities in their mission objectives, there are key differences between them when it comes to their capabilities, specifications, and applications. With the support of the ASI and DLR, hyperspectral datasets have been collected during the second half of July 2023. The ASI-PRISMA dataset considered in this work includes one image of the test area acquired on 15 July 2023; the DLR-EnMAP dataset is composed of two images collected on 14 and 22 July 2023. Both datasets were acquired under similar weather conditions (Table 1) and the sky was cloud-free during this arid period [25].

Table 1. Basic information about the hyperspectral images used.

Mission	Date	Filename	Quicklook
ASI-PRISMA	15 July 2023	PRS_L2D_STD_20230715101537	
DLR-EnMAP	14 July 2023	ENMAP01-L2A-DT0000026975_20230714T105257Z	
DLR-EnMAP	22 July 2023	ENMAP01-L2A-DT0000028486_20230722T105956Z	
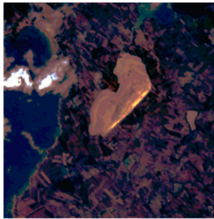
During the same period, a field campaign was deployed (18 July 2023), completing the ground measurements, which started at the beginning of June 2023 and finished in September 2023. This paper is focused on the ground dataset collected in between the satellites' passes. Ground truth spectra were collected by the spectrometer ASD FieldSpec 3 Pro [17], in the range of 0.4–2.5 μm, at the SPp (Figure 1).
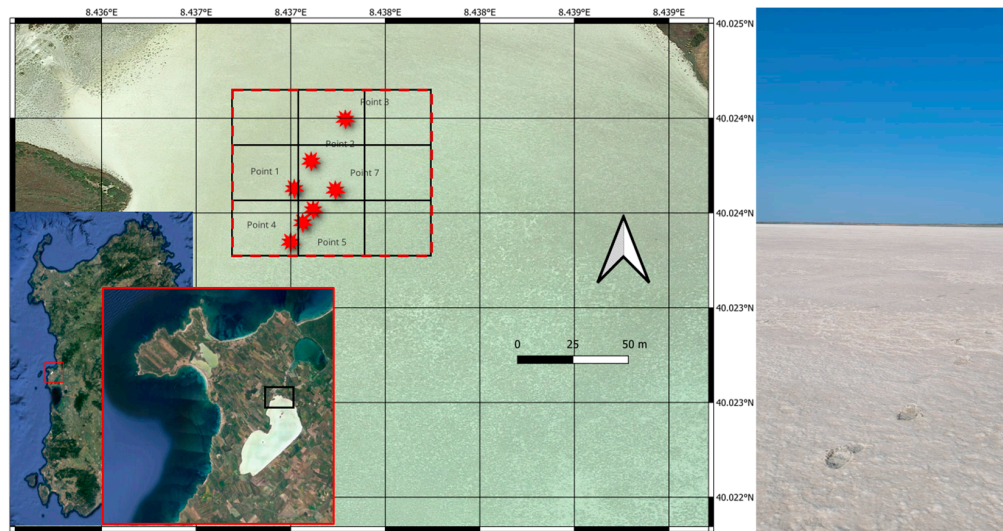
Figure 1. Geographical location of the SPp and the distribution of the sampled points within the area corresponding to the analyzed pixels belonging to the ASI-PRISMA and DLR-EnMAP. On the right, a panorama of the pond to highlights its morphology and relative homogeneity. Red stars indicate the localization of ground truth.

The SPp is located on the Sinis peninsula (West Sardinia), near the villages of San Vero Milis and Riola Sardo, and it is the largest temporary pond in Sardinia (Figure 1). It occupies a flat-bottomed interdunal depression where rainwater collects. The basin, with a maximum depth of 1 m and an average depth of 40 cm, is characterized by an absence of tributaries and emissaries, indeed it is an independent basin from the other pond areas present in the area. During the summer period, strong evaporation causes the SPp to fully dry out, presenting itself as a large expanse of salt. This phenomenon is enabled by the presence of greyish-white clay sediments at the bottom of the basin, which make it practically impermeable. This prevents the infiltration of water into the subsoil and, with the subsequent evaporation, it deposits its saline content on the surface of the depression that hosts the pond [26].

The ASI-PRISMA satellite carries a hyperspectral and panchromatic payload, capturing images with global coverage. Its hyperspectral camera utilizes a prism spectrometer and acquires data in the spectral range of 0.4–2.5 μm. It includes 63 channels in the VNIR (Visible and Near-Infrared) region and 171 channels in the SWIR (Short-Wave Infrared) region. Its spectral resolution (FWHM) is ≤12 nm across all its spectral range. There is an overlap between its VNIR bands 60–63 and SWIR bands 3–6 [10,11,13] (see Table 2).

ASI-PRISMA is in a sun-synchronous orbit, with an altitude of 614 km and an inclination of 98.19°, and its LTDN (Local Time on Descending Node) is at 10:30 h. From the ASI web portal [25], under the ASI license, the dataset reported in Table 1 has been downloaded, and by means of a homemade IDL code it has been uncompressed and, after the removal of both uncalibrated bands and "duplicated" bands [27], the VNIR-SWIR stack was generated and georeferenced. The used data level is the ASI-PRISMA's standard Level 2D (L2d), which is used for ground reflectance products, atmospherically corrected by the ASI-PRISMA automatic processor (Ver. 02.05). This automatic atmospheric effect removal procedure is based on MODTRAN v 6.0 [28], using a multidimensional look-up table (LUT) approach [29] that provides Geocoded BOA Reflectance values. These data are obtained by applying atmospheric corrections and evaluating the Rayleigh scattering, gaseous absorp-

tion, water vapor absorption, and aerosol scattering present. The atmospheric corrections applied by the ASI processor include the corrections for aerosol optical thickness and water vapor and the computation of the Angstrom exponent between channels 550/705 nm and the Cloud Optical Thickness.

Table 2. ASI-PRISMA sensor characteristics [10,11,13].

Parameter	VNIR Channel	SWIR Channel	Pan Channel
Instrument characteristics	VNIR	SWIR	PAN
Spectral range	400–1010 nm	920–2505 nm	400–700 nm
Spectral resolution (FWHM)	9–13 nm	9–14.5 nm	-
Spectral bands *	63	171	1
Signal to noise ratio (SNR)	>160 (>450 at 650 nm)	>100 (>360 at 1550 nm)	>240
Ground sampling distance (GSD)	30 m	30 m	5 m
Swath width	30 km (FOV = 2.45°)		

* after stacking.

The DLR-EnMAP (Environmental Mapping and Analysis Program) is a German Earth observation satellite under the management of the DLR. It employs imaging spectroscopy to diagnostically characterize the Earth's surface and document environmental changes. The heart of the DLR-EnMAP mission lies in the HSI (Hyperspectral Imager) sensor carried by this polar-orbiting satellite. The HSI functions as a pushbroom imager, capturing the Earth's reflected signal in the VNIR-SWIR spectral range (420–2450 nm), with global coverage. The DLR-EnMAP samples 224 spectral bands, featuring intervals of 6.5 nm and 10 nm in its VNIR and SWIR channels, respectively. Its ground spatial resolution is 30 m, and its maximum swath width extends to 30 km (Table 3) [15].

Table 3. DLR-EnMAP sensor characteristics [15,16].

Parameter	VNIR Channel	SWIR Channel
Instrument characteristics	VNIR	SWIR
Spectral range	418.42–993.34 nm	901.96–2445.3050 nm
Spectral resolution (FWHM)	8.1 ± 1.0 nm	12.5 ± 1.5 nm
Spectral bands	91	133
Signal to noise ratio (SNR)	>400:1 @495 nm	>170:1 @2200 nm
Ground sampling distance (GSD)	30 m at nadir and at sea level	
Swath width	30 km (FOV 2.63° across track)	

It operates at an altitude of 653 km and inclination of 98°, equating to a period of 97 min. The used images were collected on 14 and 22 July 2023 (Table 1). They were obtained through a web portal [30] and, for the purposes of this work, the L2A has been used. Level 2A includes surface reflectances specifically tailored to land and water applications [31]. The atmospheric correction process encompasses the creation of sun glint maps for water surfaces through the identification of specular reflections. It also involves the detection and correction of haze and cirrus, the estimation of aerosol optical thickness, columnar water vapor, and the retrieval of surface reflectances after adjacency correction [31].

To obtain the ground spectra serving as references for comparing the satellite images, a Malvern Panalytical portable spectroradiometer, ASD-FieldSpec-3 Pro, was utilized. This instrument comprises three distinct spectrometers covering the spectral range of 350–2500 nm. The full-width half-maximum (FWHM) of the spectral response of the ASD at 700 nm is 3 nm, at 1400 nm it is 10 nm, and at 2100 nm it is 10 nm. Measurements were conducted using the bare fiber-optic cable with a field of view of 25°, and each measurement site was associated with GPS coordinates. The instrument's operational details are outlined in the ASD's documentation from 1994, which was subsequently updated [17]. Ground truth measurements were paired with a portable GPS, recording coordinates for each

spectrum in NMEA0183 format, as according to [17]. Reflectance measurements were collected on 18 July 2023, which encompassed 105 acquired samples distributed on an area covering approximatively 6 pixels of the ASI-PRISMA and DLR-EnMAP images. Spectralon measurements were taken to convert raw radiance to absolute reflectance. The comparison between surface reflectance values from the ASI-PRISMA and DLR-EnMPAP and the averaged value (aGT), derived from all 105 spectra to assess the ground truth against the remote-sensed data, was evaluated using various statistical parameters. Specifically, the Pearson correlation coefficient was employed to assess the correlation between reflectance estimates, (see Equation (1)), while R^2, which is the determination coefficient as calculated in Equation (2), allows us to evaluate the differences and the spread of the compared datasets.

$$\text{Pearson correlation coefficient}: \rho_{Satellite,\,aGT} = \frac{cov(satellite,\,aGT)}{\sigma_{(satellite)} * \sigma_{(aGT)}} \tag{1}$$

where *cov* is the covariance between the surface reflectances derived by satellites measurements and ground measurements, respectively, and $\sigma_{(satellite)}$ and $\sigma_{(aGT)}$ are the standard deviation of the surface reflectance derived by the satellites' measurements and ground measurements, respectively.

$$R^2 = 1 - \frac{\sum_{i=1}^n (\rho_i(satellite) - \rho_i(aGT))^2}{\sum_{i=1}^n ((\rho_i(aGT)) - \overline{\rho(aGT)})^2} \tag{2}$$

where $\rho(satellite)$ is the reflectance estimated by means of the ASI-PRISMA and DLR-ENMAP and $\rho(aGT)$ is the averaged ground truth, respectively, for each spectral band.

3. Results and Discussion

This section presents the outcomes of the comparisons between products gathered from official datasets. Remembering that the standard L1 TOA radiance and L2 BOA reflectance products provided by ASI and DLR were used, analyses of both BOA reflectance and TOA radiance encompass the entire spectrum within the range 400 to 2500 nm. The L2 BOA reflectance values have been compared with the ground truth acquired on the 18 July 2023 from the SPp. Subsequently, the reflectance spectra were assessed and juxtaposed with those obtained from the FieldSpec spectrometer during the field survey.

The radiance trends for the DLR-EnMAP and ASI-PRISMA have different behaviors in different sections of the electromagnetic spectrum. In the VNIR region, there is a clear coincidence between 15 July ASI-PRISMA (acquired at 10:15:37 local time) and 14 July DLR-EnMAP (acquired at 10:52:57 local time) data (respectively, the red and green lines in Figure 2). The 22 July DLR-EnMAP (acquired at 10:59:56 local time) data have, in the VNIR region, higher values (the black line in Figure 2). On the other hand, the SWIR bands present an overlap between the two DLR-EnMAP radiances, which are slightly overestimated with respect to that of the ASI-PRISMA. Analyzing the differences between these radiances, they are greater in the VNIR region and become almost null in the SWIR region (Figure 2).

The emphasized differences could be related to two factors: the sun's irradiance, which varies during the daytime and on different days (as between the 14, 15, and 22 July), and the aerosol loading over the area. A further unestimated contribution could be related to slight differences in atmospheric conditions (i.e., water vapor). With the aim of assessing these differences, several model simulations have been performed by employing the MODTRAN radiative transfer model. The setup for these model simulations is reported in Table 4.
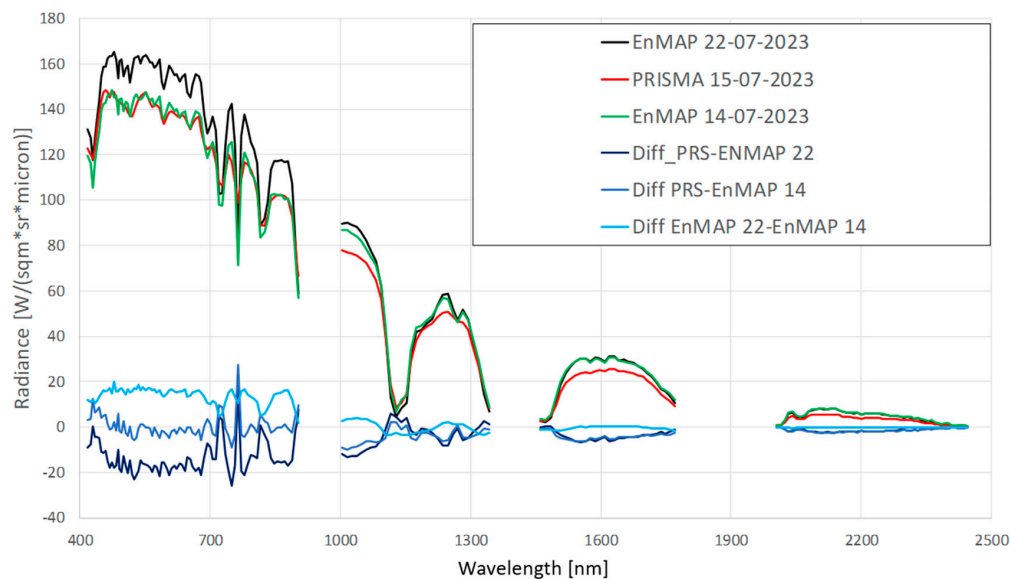
Figure 2. Relation between DLR-EnMAP (black line and green line are, respectively, 22 and 14 July 2023) and ASI-PRISMA (red line, 15 July 2023) radiances. The lines in different shades of blue indicate the values of the differences between the different combinations of remote-sensed radiance.

Table 4. Setup of MODTRAN simulations.

Simulation ID	Day	Local Time (hh:mm)	Surface Albedo	Aerosol Optical Thickness	Viewing Angle
#1	15 July	10:15	aGT	0.17 *	−12.31° (PRISMA)
#2	15 July	10:15	aGT	0.25 **	−12.31° (PRISMA)
#3	15 July	11:00	aGT	0.17 *	−12.31° (PRISMA)
#4	22 July	11:00	aGT	0.17 *	+14.71° (EnMAP)

*, from L2 ASI-PRISMA data; **, simulated to test the effect of the aerosol loading.

The results of the simulations, in terms of their TOA radiance, are reported in Figure 3. The strong effect of the AOT parameter, with radiance differences up to 10 $W*m^{-2}*sr^{-1}*\mu m^{-1}$ in the VNIR region, is evident in the entire range of 400–1800 nm (Figure 3A). Also, the difference in the time of acquisition (10:15 vs. 11:00 L.T.), with a great difference in solar irradiance, leads to important variations in the TOA radiances (Figure 3B). Finally, the simulations do not indicate any significant effects when only changing the day while holding the other parameters constant (AOT, time, ground reflectance) (Figure 3C).

It is important to remember that, in this paper, we used standard BOA data as they are furnished by the data providers (both DLR and ASI) and, therefore, we do not control the inversion procedure adopted [1,29]. When adopting these procedures and examining the reflectance characteristics at 780 nm, it is evident that the DLR-EnMAP atmospheric removal effect L2 algorithm does not adequately correct for O_2 atmospheric absorption with respect to the ASI-PRISMA algorithm, which achieves a more precise correction. At the same time, the presence of saw-tooth features in the ASI-PRISMA data may be attributed to potential over-correction by the used algorithm.

Regarding the ASI-PRISMA feature at 1260 nm (the red curve) that is not present in the DLR-EnMAP data, it appears to be an excessive correction for CO_2. At this wavelength (1260 nm), this feature is not as pronounced in the PRISMA radiance as observed in the ENMAP data in Figure 2.
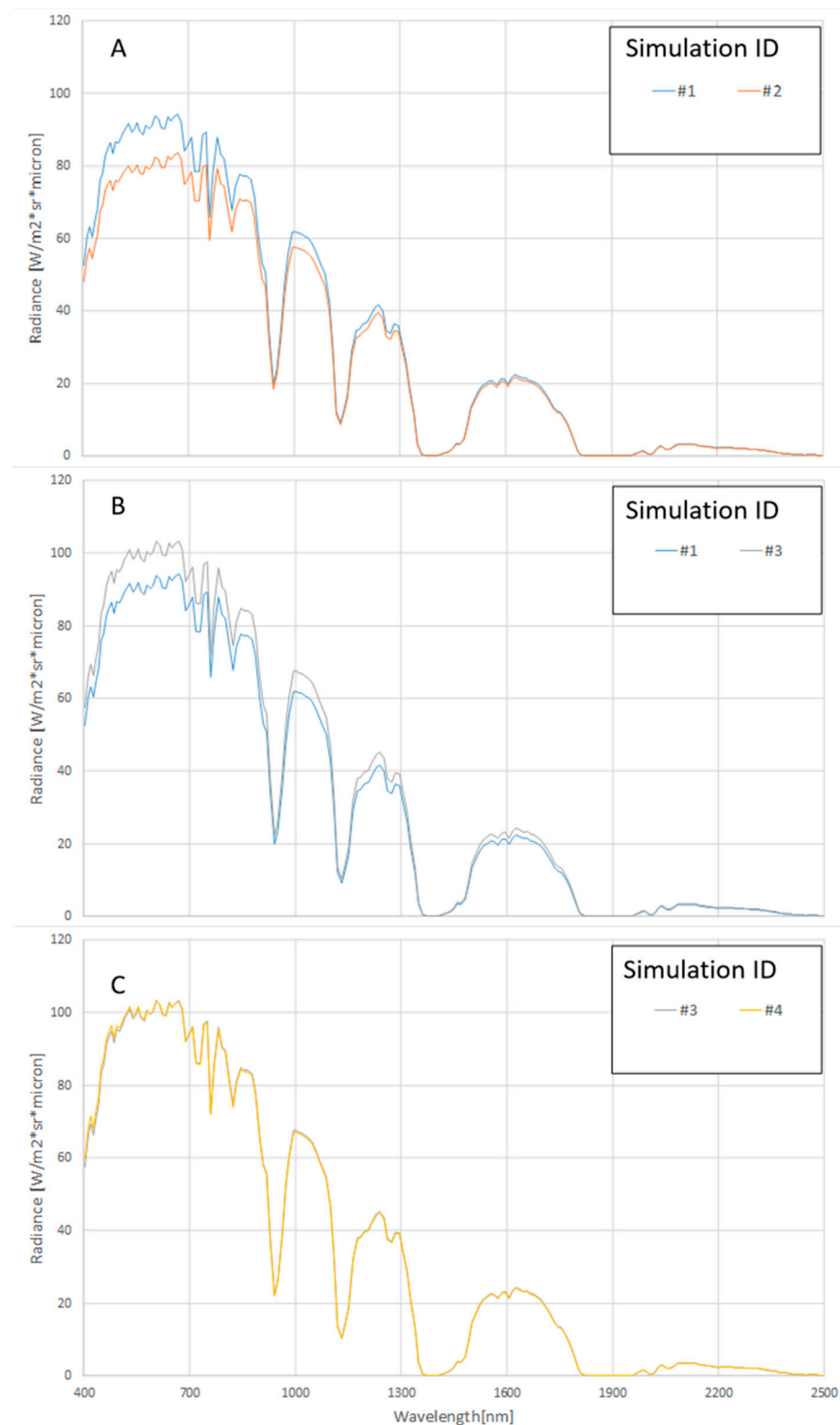
Figure 3. Spectral profiles of TOA radiances simulated by means of the MODTRAN model. In accordance with Table 4, panel (**A**) shows the comparison between Simulation ID #1 and #2; panel (**B**) shows the comparison between Simulation ID #1 and 3; and panel (**C**) shows the comparison between Simulation ID #3 and #4.

The standard BOA reflectance products (Figure 4), sampled on the same area of interest (Figure 1) as where the ground truth was collected, show that the ground reflectance was

properly estimated. The three different curves have very similar trends, overlapping each other in different parts of the spectrum. Reported in the same figure are the absolute error, calculated as reported in Equation (3),

$$(Refl_{max} - Refl_{mean})/2 \tag{3}$$

and the relative errors, calculated according to Equation (4):

$$\frac{Mean(\Sigma reflectance)}{Absolute\ Error} \tag{4}$$

Both errors (absolute and relative) are relevant to the EO data collected.
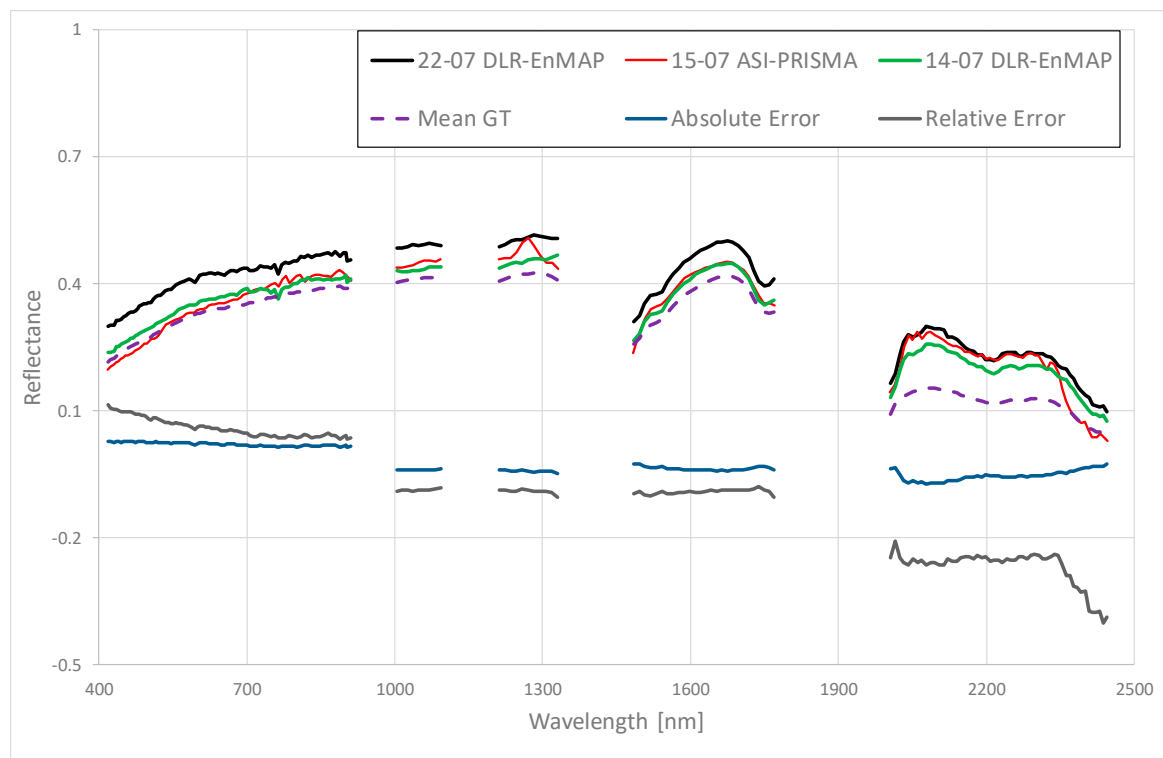
Figure 4. Absolute (dark blue) and relative (dark grey) errors between remote-sensed reflectance data (DLR-EnMAP: black line and green line, respectively, 22 and 14 July 2023, and ASI-PRISMA: red line, 15 July 2023) and aGT (dashed purple line). The absolute error is equal to Equation (3) and the relative errors is equal to Equation (4).

The two datasets acquired on 14 and 15 July run in parallel, with similar values up to 1800 nm. In the same range, the data acquired on 22 July are slightly overestimated, while, in the 2000–2300 nm spectral range, they run almost parallel with the ASI-PRISMA data included into the two DLR-EnMAP datasets, recording a drop of the ASI-PRISMA signal after 2300 nm.

The absolute mean difference between the reflectance values estimated by the ASI-PRISMA and DLR-EnMAP, for the test area, is around −0.015, with a minimum of −0.07 (around 2100 nm) and a maximum of −0.027 at the beginning of the spectral range. The average relative mean difference between the reflectance values estimated by the ASI-PRISMA and DLR-EnMAP, for the test area, is around −0.075, with a minimum of −0.4 close to the end of the SWIR region and a maximum of 0.11 in the first channel of VNIR region (Figure 4). The difference between the averaged remote-sensed data and the ground truth is 0.05, with the maximum difference reached in the SWIR region (0.12) (Figure 5).
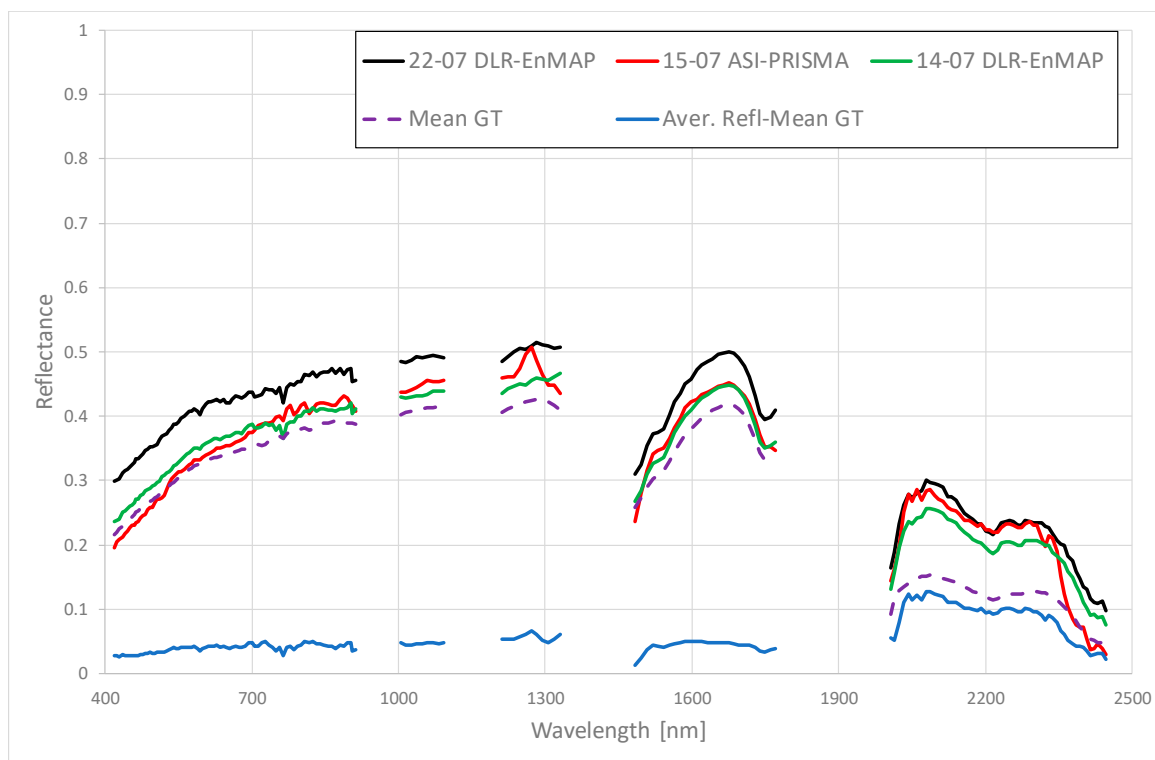
Figure 5. Black, green, red, and dotted purple curves as in Figure 4; the light blue curve is the difference between the averaged EO data and the aGT. This difference has an averaged value of 0.05, with the maximum difference reached in the SWIR region (0.12).

Although the weather conditions on individual days were not different, the trend over the period of 14–22 July indicates a slight increase in cloud cover. This evolution makes the data for 22 July, although consistent with that of the 14th with respect to the ground acquisitions of the 18, less statistically rigorous.

On the 18 July, a field campaign was deployed to collect ground truth data by means of a portable spectroradiometer suitable for acquiring spectra in the same wavelength range as the ASI-PRISMA and DLR-EnMAP. Measurements of reflectances were collected on 18 July 2023 and on this day the weather was excellent, with an absence of cloud over the site and with almost zero knots of wind, allowing for data collection over 7 different sites (Figure 4), which can be considered numerically adequate considering the small variation in spectral behavior (Figure 6A) of the area considered (Figure 1, where a qualitative representation of both the area's homogeneity and the clear sky is reported).

Table 5 shows the names of the measuring points and the number of spectra acquired.

Table 5. Naming, coordinates, and number of samples collected during the 18 July field survey.

Point Number (Figure 1)	Longitude (E)	Latitude (N)	Number of Samples	Ground Truth Acquisition Time (Local Time)	White Reflectance Acquisition Time (Local Time)
Point 1	8.4370193°	40.023628°	15	12:28–12:30	
Point 2	8.4371088°	40.023773°	15	12:31–12:33	
Point 3	8.4372896°	40.023995°	15	12:34–12:36	12:27
Point 4	8.4370000°	40.023346°	15	12:38–12:40	
Point 5	8.4370639°	40.023448°	15	13:08–13:10	
Point 6	8.4371193°	40.023516°	15	13:11–13:13	13:07
Point 7	8.4372368°	40.023621°	15	13:15–13:18	
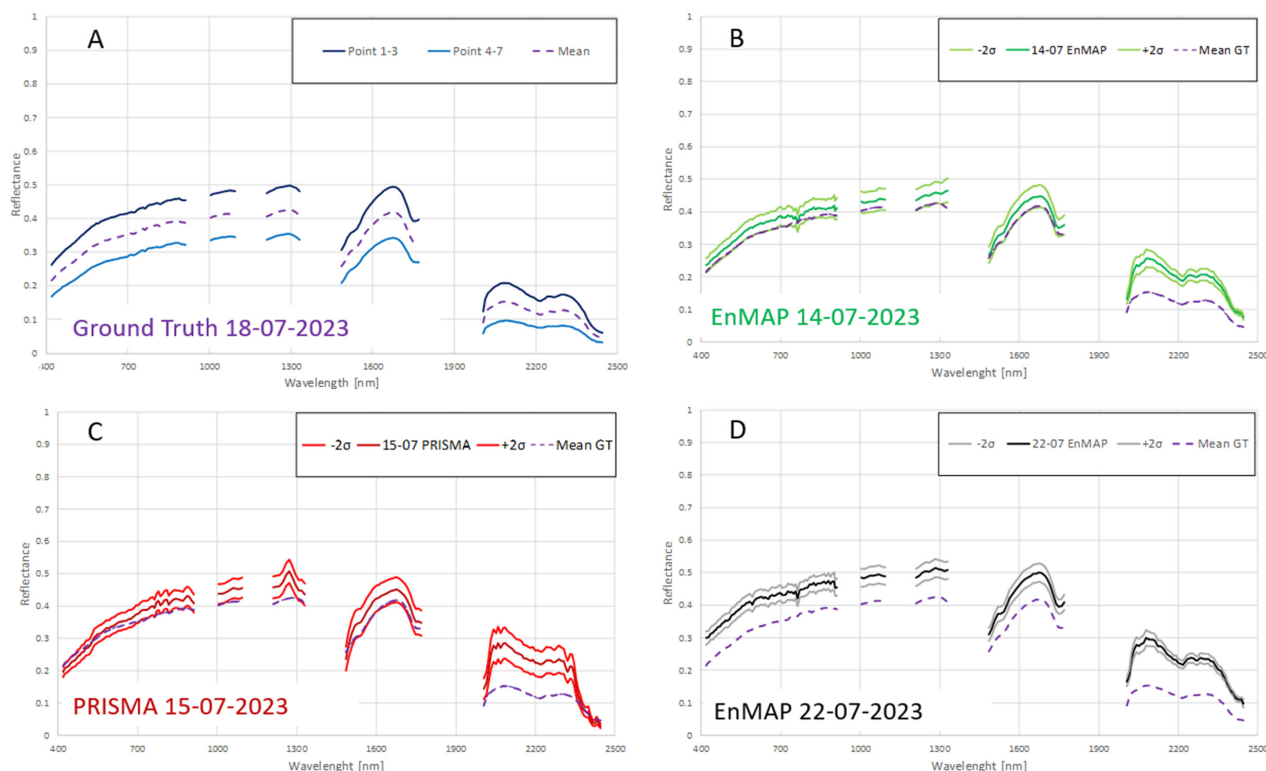
Figure 6. Ground reflectance data collected using a field spectroradiometer. Dark blue line is the average of the first three points, while the light blue is the average of the last four points. The dashed purple line is the average of the previous two lines and will be used for the further comparison (**A**). (**B**) comparison of the DLR-EnMAP reflectance values acquired on 14 July relevant to the pixel located at the coordinates reported in Table 4; (**C**) Comparison of the ASI-PRISMA reflectance values relevant to the pixel located at the coordinates reported in Table 4; (**D**) comparison of the DLR-EnMAP reflectance values acquired on 22 July relevant to the pixel located at the coordinates reported in Table 4.

The spectral data at the sites were obtained using a consistent methodology. For each measurement, the distance between the fiber-optic cable and the target was maintained as constant as possible. This uniform distance was also upheld across various sites. Fifteen samples were collected at each point, and the mean value was calculated from these measurements. Upon analyzing the collected spectra (Figure 4), it is evident that the sampled sites exhibit similar trends, albeit with varied absolute values. These values peak at 0.5 around 1600 nm and decline below 0.2 in the latter part of the SWIR region.

The weather conditions were constant during the first three samplings, worsening slightly immediately afterwards (points 4–7). Indeed, optimization and white reference (Table 4) collection ASD procedures have been followed to keep the data, as much as possible, comparable. Because of the coherence in the data, in the following we use the aGT. The dashed purple line represents the average of the 105 samples collected on 18 July 2023 at the SPp.

The ASI-PRISMA data were collected three days before the field survey. Considering all the remote data analyzed, these was the closest in time with respect to the on-the-ground spectral sampling. In Figure 6 three curves are reported: the dark red represents the mean value of the ASI-PRISMA reflectance value, measured according to the pixel included in the bounding box presented in Figure 1 and centered on the site position reported in Table 4; the red curves are representative of ±2σ (STDv).

From 400 nm up to 1750 nm the aGT runs between the ASI-PRISMA mean value and its −2σ, while from 1950 nm and 2300 nm the aGT value is significantly lower than the −2σ ASI-PRISMA trend. In the final SWIR spectral range, the ASI-PRISMA value

is overestimated with respect to the aGT (Figure 4). The ASI-PRISMA image presents a "shark teeth" absorption feature from 780 nm up to 820 nm, due to an improper correction of water vapor not present in the ground truth data. Also, at 1250 nm, the ASI-PRISMA presents a peak which does not correspond to any feature of the aGT data (Figure 6A). These differences can be attributed to the atmospheric contribution removal process, passing from TOA radiance to BOA reflectance, which can introduce artefacts during the generation of a standard product.

Differences occur between the aGT and the relevant DLR-EnMAP spectra, respectively, the 14th (Figure 6B) and 22 July (Figure 6D) datasets; it is possible to underline how nearly parallel the aGT is to the 14 July -2σ DLR-EnMAP data from 400 up to 1750 nm, and, similarly to the ASI-PRISMA data in the SWIR region, there is an overestimation of the remote-sensed data with respect to the aGT. The DLR-EnMAP does not show a signal drop after 2300 nm as the ASI-PRISMA does.

Comparing the aGT with the 22 July DLR-EnMAP data (Figure 6D), an overestimation of the space data response is constant along the full spectral range, with different absolute values. The mean DLR-EnMAP response and the $\pm2\sigma$ response are, in general, higher than the aGT.

Both DRL images (Figure 6B,D) present a narrow absorption feature around 780 nm (where ASI-PRISMA presents the "shark teeth") and also, in these cases, it represents a feature not present in the data collected with the portable spectroradiometer. For this reason it has been attributed to the atmospheric correction procedure adopted to generate the DLR-EnMAP standard surface reflectance product, and in particular to a water vapor removal effect that was not properly performed.

With the aim of comparing the reflectance values of the L2 products, three spectral sectors are considered (see Table 6) for the DLR-EnMAP on the 14th and the ASI-PRISMA on the 15 July.

Table 6. Mean reflectance values from the EnMAP and PRISMA in the considered spectral sectors; their absolute differences are also reported.

Wavelength Sector (Micron)	EnMAP Mean	PRISMA Mean	Absolute Difference
0.4–0.911	0.3479	0.3362	0.0116
1.003–1.769	0.4097	0.4183	−0.0086
2.005–2.445	0.1901	0.1957	−0.0057

The DLR-EnMAP reflectance overestimates the ASI-PRISMA's from 400 up to 1790 nm; the overall mean difference is about −0.0009 and is contained in the variability of the DLR-EnMAP values, corresponding to 0.044 (equivalent to 2 standard deviations). Despite the drop in the ASI-PRISMA SWIR signal due to the atmospheric correction procedure applied in the BOA-TOA passage, there is a relative overestimation of the ASI-PRISMA values between 2005 and 2445 nm. Therefore, the reflectance values are quantitatively compared by wavelength-pairing remote-sensed data with the ground truth using the above-mentioned statistical parameters. Scatter plots of the cross comparisons are reported in Figure 7.

In the scatter plots of the satellite/ground truth reflectance values, the light yellow line indicates the regression line. The inset reports the Pearson coefficient and R^2 values. The resulting values of the Pearson coefficient and R^2 computed for each hyperspectral dataset with respect to the ground truth value are reported in Table 7.
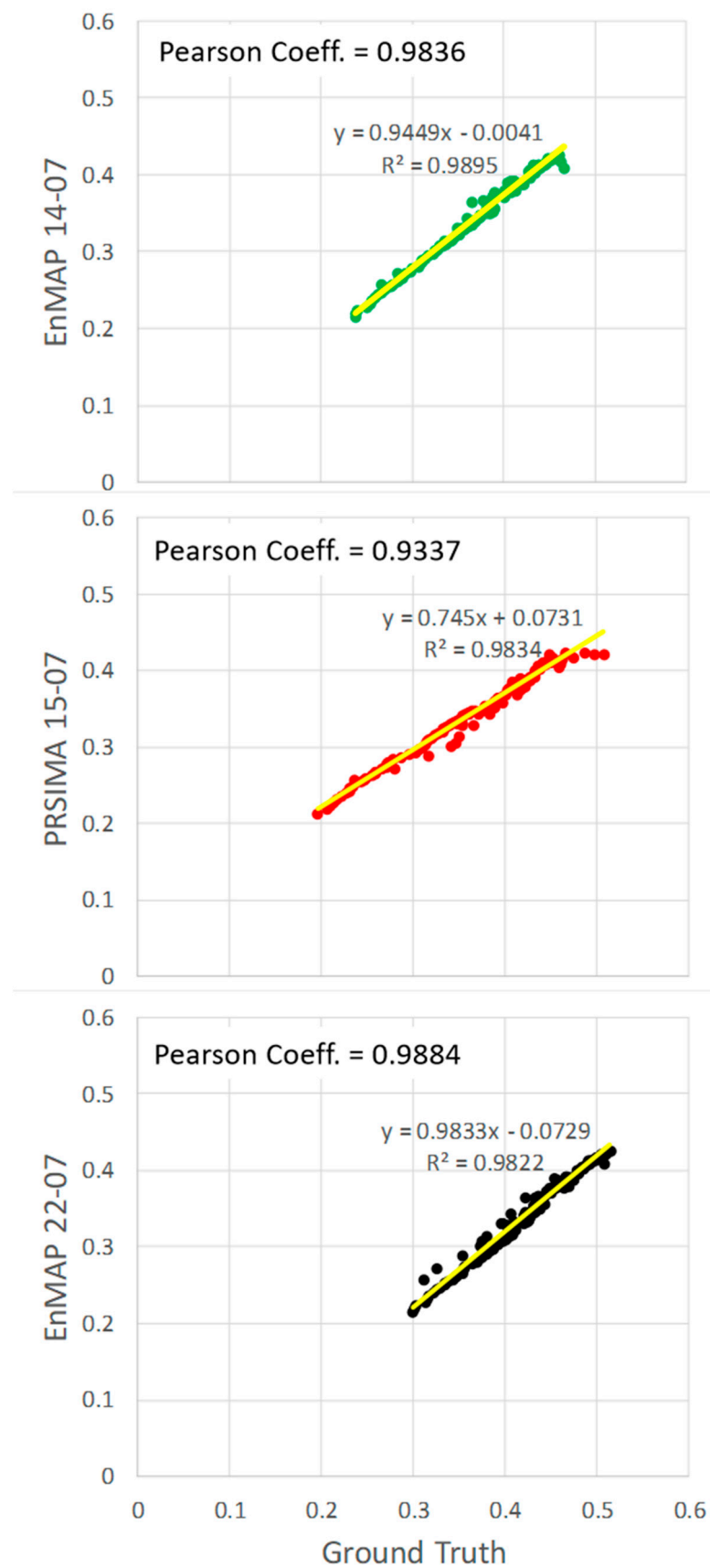
Figure 7. 400–1700 nm scatter plot of DLR-EnMAP, ASI-PRISMA, and FieldSpec reflectance values. Each point represents the comparison between radiances for each spectral channel. The relative regression lines are also reported (yellow lines).

Table 7. Mean reflectance values of EnMAP and PRISMA in the considered spectral sectors; their absolute differences are also reported.

	EnMAP22 vs. aGt	PRISMA 15 vs. aGt	EnMAP 14 vs. aGt
Pearson Coefficient	0.9884	0.9337	0.9836
R^2	0.9833	0.9834	0.9895

The Pearson correlation coefficient assesses the linear correlation between two variables, irrespective of scaling factors and offsets. With a value exceeding 0.8, indicating a highly significant correlation, it is noteworthy that all surface reflectance values derived from the various sensors exhibit a very strong correlation.

The most substantial correlations were observed for the DLR-EnMAP 22nd and DLR-EnMAP 14th data, registering at 0.9884 and 0.9836, respectively. Conversely, the weakest correlation (0.9337) was observed for the ASI-PRISMA on 15 July. The decreased correlation observed in the PRISMA data might stem from variations in behavior between the ground truth and BOA data within the visible spectrum range of 400–900 nm. Although the EnMAP reflectance values are higher than the ground truth, they exhibit a similar shape. In contrast, the PRISMA data tend to underestimate the ground truth within the 400–500 nm range and overestimate it within the 500–900 nm range and present a lower correlation due to the presence of an artifact near 1280 nm.

4. Conclusions

We used two types of satellite datasets to compare them with a reference dataset acquired ad hoc. The "Sale 'e Porcus" pond has been used as a reference site due to its suitable morphological and compositional characteristics. The standard reflectance products generated by the Italian and German Space agencies and the ground truth data acquired on the dried pond comprised the backbone of this paper. This comparison of surface reflectances derived from the ASI-PRISMA and DLR-EnMAP shows that the sensors have a very comparable response in terms of the measurements collected by independent instruments. These data have a high value to their correlation coefficient, as highlighted by the statistical indices adopted.

The considered test site is the "Sale 'e Porcus" pond (Sardinia, Italy), which is a flat and homogeneous area of about 3.5 km². The site is located approximately at sea level, and due to its morphological and compositional characteristics it is suitable also for calibration purposes, as it is totally dried up for several months per year. The spectra profiles of the ASI-PRISMA and DLR-EnMAP's TOA radiance were compared and the relevant BOA reflectances have been analyzed with respect to the local ground truth data collected on the pond.

The Pearson correlation coefficient is very high for the data from both the VNIR and SWIR spectral ranges. Lower R^2 and Pearson coefficient values are attributed to the instruments' response in the SWIR spectral range and to the capability of these instruments to resolve low reflectance values. Both remote-sensed data overestimated the SWIR response when compared with the ground truth. Among the satellites' data, the DLR-EnMAP shows higher values with respect to the ASI-PRISMA for the full spectral range.

Apart from the SWIR region, the ground truth lies within or very close to the 14 July DLR-EnMAP and 15 July ASI-PRISMA data, with a variability of $\pm 2\sigma$ (STDv) (Figure 4). The agreement between the reflectance values estimated by the aGT and the entire EO dataset on the SPp, the selected ROI, was contained to a relative mean difference smaller than 0.12 (Figure 5).

The timings of the satellite measurements are very close to each other, as are those of the ground truth data, which were acquired in a time window close to the satellite passages; this timing ensured very similar atmospheric conditions and no variations in surface conditions.

Finally, the FieldSpec measurements also confirmed the great quality of the ASI-PRISMA and DLR-EnMAP reflectance estimations. The difference between the remote-sensed data and the ground truth is about 0.05.

Although this work was not intended to evaluate the ASI and DLR sensors' performances, this study highlights the necessity of enlarging this case study by following two main strategies: by enlarging the statistical population by using more remote-sensed data and increasing the statistical weight of the ground truth data and by applying a similar approach to different environmental conditions. Despite the authors' belief that the SPp is suitable for CAL/VAL purposes, it is necessary to improve our knowledge of local characteristics, especially during the satellites' passage.

Author Contributions: Conceptualization, M.M.; methodology, M.M., M.C. and M.S.; formal analysis, M.F.B. and V.R.; data curation, V.R., M.T.M. and M.C.; writing—original draft preparation, M.M.; writing—review and editing, M.F.B. and M.T.M. All authors have read and agreed to the published version of the manuscript.

Data Availability Statement: Not applicable.

Conflicts of Interest: The authors declare no conflicts of interest.

References

1. Lorenz, S.; Zimmermann, R.; Gloaguen, R. The Need for Accurate Geometric and Radiometric Corrections of Drone-Borne Hyperspectral Data for Mineral Exploration: MEPHySTo—A Toolbox for Pre-Processing Drone-Borne Hyperspectral Data. *Remote Sens.* **2017**, *9*, 88.
2. Niyogi, D.; Jamshidi, S.; Smith, D.; Kellner, O. Evapotranspiration Climatology of Indiana, USA Using In-Situ and Remotely Sensed Products. *J. Appl. Meteorol. Clim.* **2020**, *59*, 2093–2111. [CrossRef]
3. Jamshidi, S.; Zand-Parsa, S.; Jahromi, M.N.; Niyogi, D. Application of A Simple Landsat-MODIS Fusion Model to Estimate Evapotranspiration over A Heterogeneous Sparse Vegetation Region. *Remote. Sens.* **2019**, *11*, 741. [CrossRef]
4. Jamshidi, S.; Zand-Parsa, S.; Pakparvar, M.; Niyogi, D. Evaluation of Evapotranspiration over a Semiarid Region Using Multiresolution Data Sources. *J. Hydrometeorol.* **2019**, *20*, 947–964. [CrossRef]
5. Chander, S.; Gujrati, A.; Krishna, A.V.; Sahay, A.; Singh, R. Remote sensing of inland water quality: A hyperspectral perspective. In *Hyperspectral Remote Sensing*; Elsevier: Amsterdam, The Netherlands, 2020; pp. 197–219.
6. Hulley, G.C.; Duren, R.M.; Hopkins, F.M.; Hook, S.J.; Vance, N.; Guillevic, P.; Johnson, W.R.; Eng, B.T.; Mihaly, J.M.; Jovanovic, V.M.; et al. High spatial resolution imaging of methane and other trace gases with the airborne Hyperspectral Thermal Emission Spectrometer (HyTES). *Atmos. Meas. Tech.* **2016**, *9*, 2393–2408. [CrossRef]
7. Romaniello, V.; Spinetti, C.; Silvestri, M.; Buongiorno, M.F. A Methodology for CO_2 Retrieval Applied to Hyperspectral PRISMA Data. *Remote Sens.* **2021**, *13*, 4502. [CrossRef]
8. Bagheri, N.; Mohamadi-Monavar, H.; Azizi, A.; Ghasemi, A. Detection of Fire Blight disease in pear trees by hyperspectral data. *Eur. J. Remote Sens.* **2017**, *51*, 1–10. [CrossRef]
9. Loizzo, R.; Guarini, R.; Longo, F.; Scopa, T.; Formaro, R.; Facchinetti, C.; Varacalli, G. Prisma: The Italian Hyperspectral Mission. In Proceedings of the IGARSS 2018—2018 IEEE International Geoscience and Remote Sensing Symposium, Valencia, Spain, 22–27 July 2018; Institute of Electrical and Electronics Engineers (IEEE): Piscataway, NJ, USA, 2018; pp. 175–178.
10. Coppo, P.; Brandani, F.; Faraci, M.; Sarti, F.; Dami, M.; Chiarantini, L.; Ponticelli, B.; Giunti, L.; Fossati, E.; Cosi, M. Leonardo spaceborne infrared payloads for Earth observation: SLSTRs for Copernicus Sentinel 3 and PRISMA hyperspectral camera for PRISMA satellite. *Appl. Opt.* **2020**, *59*, 6888–6901. [CrossRef] [PubMed]
11. Cogliati, S.; Sarti, F.; Chiarantini, L.; Cosi, M.; Lorusso, R.; Lopinto, E.; Miglietta, F.; Genesio, L.; Guanter, L.; Damm, A.; et al. The PRISMA imaging spectroscopy mission: Overview and first performance analysis. *Remote Sens. Environ.* **2021**, *262*, 112499. [CrossRef]
12. Heller Pearlshtien, D.; Pignatti, S.; Greisman-Ran, U.; Ben-Dor, E. PRISMA sensor evaluation: A case study of mineral mapping performance over Makhtesh Ramon, Israel. *Int. J. Remote Sens.* **2021**, *42*, 5882–5914. [CrossRef]
13. Pignatti, S.; Amodeo, A.; Carfora, M.F.; Casa, R.; Mona, L.; Palombo, A.; Pascucci, S.; Rosoldi, M.; Santini, F.; Laneve, G. PRISMA L1 and L2 Performances within the PRISCAV Project: The Pignola Test Site in Southern Italy. *Remote Sens.* **2022**, *14*, 1985. [CrossRef]
14. Romaniello, V.; Silvestri, M.; Buongiorno, M.F.; Musacchio, M. Comparison of PRISMA Data with Model Simulations, Hyperion Reflectance and Field Spectrometer Measurements on 'Piano delle Concazze'(Mt. Etna, Italy). *Sensors* **2020**, *20*, 7224. [CrossRef] [PubMed]
15. Available online: https://www.enmap.org/ (accessed on 13 March 2024).

16. Storch, T.; Honold, H.P.; Chabrillat, S.; Habermeyer, M.; Tucker, P.; Brell, M.; Ohndorf, A.; Wirth, K.; Betz, M.; Kuchler MMühle, H.; et al. The EnMAP imaging spectroscopy mission towards operations. *Remote Sens. Environ.* **2023**, *294*, 113632. [CrossRef]
17. Analytical Spectral Devices, Inc. 2023. Available online: https://www.malvernpanalytical.com/en (accessed on 13 March 2024).
18. Asadzadeh, S.; de Souza Filho, C.R. A review on spectral processing methods for geological remote sensing. *Int. J. Appl. Earth Obs. Geoinf.* **2016**, *47*, 69–90. [CrossRef]
19. Yu, H.; Kong, B.; Wang, Q.; Liu, X.; Liu, X. Hyperspectral remote sensing applications in soil: A review. *Hyperspectral Remote Sens.* **2020**, 269–291.
20. Vignesh, K.M.; Kiran, Y. Comparative analysis of mineral mapping for hyperspectral and multispectral imagery. *Arab. J. Geosci.* **2020**, *13*, 160. [CrossRef]
21. Di Gennaro, S.F.; Toscano, P.; Gatti, M.; Poni, S.; Berton, A.; Matese, A. Spectral comparison of UAV-Based hyper and multispectral cameras for precision viticulture. *Remote Sens.* **2022**, *14*, 449. [CrossRef]
22. Calvini, R.; Ulrici, A.; Amigo, J.M. Growing applications of hyperspectral and multispectral imaging. *Data Handl. Sci. Technol.* **2019**, *32*, 605–629.
23. Available online: https://prisma.asi.it (accessed on 13 March 2024).
24. Available online: https://planning.enmap.org/ips/app#home (accessed on 13 March 2024).
25. Available online: https://www.meteoblue.com/it/tempo/historyclimate/weatherarchive/san-vero-milis_italia_3167212?fcstlength=1m&year=2023&month=7 (accessed on 13 March 2024).
26. Massoli Novelli, R.; Mocci Demartis, A. *Le Zone Umide Della Sardegna. Stagni–Lagune–Laghi–Paludi*; Editoriale Olimpia: Florence, Italy, 1989.
27. PRISMA Products Specification Document Issue 2.3 Date 12/03/2020. Available online: https://prisma.asi.it/missionselect/docs/PRISMA%20Product%20Specifications_Is2_3.pdf (accessed on 13 March 2024).
28. Berk, A.; Conforti, P.; Kennett, R.; Perkins, T.; Hawes, F.; van den Bosch, J. MODTRAN6: A Major Upgrade of the MOD-TRAN Radiative Transfer Code. Available online: https://www.spiedigitallibrary.org/conference-proceedings-of-spie/9088/1/MODTRAN6--a-major-upgrade-of-the-MODTRAN-radiative-transfer/10.1117/12.2050433.short?SSO=1 (accessed on 10 June 2020).
29. ASI—Italian Space Agency. PRISMA Algorithm Theoretical Basis Document (ATBD), Issue 1, Date 14/12/2021. 2021. Available online: https://prisma.asi.it/missionselect/docs/PRISMA%20ATBD_v1.pdf (accessed on 29 November 2023).
30. Available online: https://planning.enmap.org/ips/app#userportal (accessed on 13 March 2024).
31. DLR—Deutsches Zentrum für Luft- und Raumfahrt e.V.- Level 2A Processor (Atmospheric Correction over Land) ATBD. Issue 2.4 Date 07.09.2023. Available online: https://www.enmap.org/data/doc/EN-PCV-TN-6007_Level_2A_Processor_Atmospheric_Correction_Land.pdf (accessed on 4 December 2023).